Journal of Zhejiang University-SCIENCE A
www.jzus.zju.edu.cn; www.springer.com/journal/11582
E-mail: jzus_a@zju.edu.cn

Research Article
https://doi.org/10.1631/jzus.A2600028

Bioinspired shape memory alloy-driven underwater soft robot enabled by pectoral–caudal-fin coordination and passive liquid thermal management

Xia HUANG[1], Guan HUANG[1], Zhigang DING[2], Shaojie GU[3], Jun DING[1], Yanhong PENG[1,3,4]✉, Zebing MAO[5]✉

[1]*College of Mechanical Engineering, Chongqing University of Technology, Chongqing 400054, China*
[2]*Nantong Public Transportation Group Co., Ltd., Nantong 226000, China*
[3]*Magnesium Research Center, Kumamoto University, Kumamoto 860-8555, Japan*
[4]*Department of Information and Communication Engineering, Graduate School of Engineering, Nagoya University, Nagoya 464-8603, Japan*
[5]*State Key Laboratory of Fluid Power and Mechatronic Systems, Zhejiang University, Hangzhou 310058, China*

Abstract: Bioinspired robotic fish can provide compliant, low-noise underwater locomotion, but compact shape memory alloy (SMA)-driven designs often suffer from slow response and poor fatigue life. We propose a grass-carp-inspired pectoral–caudal-fin (PCF) soft robot to realize body caudal-fin (BCF) and median paired-fin (MPF) multimodal swimming and specifically improve SMA performance via embedded thermal management. The robot integrates an SMA spring caudal-fin actuator and a large-strain SMA pectoral-fin actuator within a watertight compliant body and adopts a sealed-cavity liquid-cooling scheme. Experiments show markedly enhanced actuation bandwidth and durability, enabling stable multimodal locomotion with a 45.67 mm/s peak speed and 9.12 (°)/s peak turning rate, plus ultrasonic-based obstacle avoidance at 20 cm. The results suggest a compact pathway to resilient, versatile underwater soft robots for long-duration operation in cluttered environments.

Key words: Underwater soft robot; Bionic robot; Shape memory alloy (SMA); Pectoral–caudal-fin (PCF) coordination; Passive liquid thermal management; Multimodal locomotion

1 Introduction

Underwater robots are of growing importance for inspection (Nauert and Kampmann, 2023; Liu RN et al., 2025), monitoring (Chutia et al., 2017), and exploration (Xanthidis et al., 2022; Huang et al., 2026) in confined or fragile aquatic environments where safety, compliance, and efficiency are critical (Sahoo et al., 2024). Compared with conventional rigid-bodied robots, soft robots offer superior compliance and adaptability, enabling safer physical interaction (Mao et al., 2025; Peng et al., 2025, 2026), enhanced environmental compatibility, and robust locomotion (Liu X et al., 2025) in unstructured or confined environments. Among them, robotic fish are attractive because fish-like morphologies and fin-driven propulsion can deliver low-noise, high-maneuverability locomotion compared with propeller-based systems (Ding et al., 2024; Varnousfaderani et al., 2025; Li et al., 2026). However, achieving both efficient cruising and agile maneuvering typically requires coordinated use of body caudal-fin (BCF) (Sfakiotakis et al., 1999) and median paired-fin (MPF) (Cui et al., 2023) propulsion, which remains challenging under tight constraints on actuation volume, sealing, and onboard integration. Consequently, current research increasingly targets soft (Li et al., 2022; Ding et al., 2024; Sheng et al., 2025) and smart-material (Liu et al., 2024; Wang et al., 2026) actuation strategies that can provide multimodal swimming while preserving compactness and mechanical compliance. This trend motivates a closer examination of how actuator thermal dynamics, structural compliance, and

✉ Yanhong PENG, yhpeng@nagoya-u.jp
Zebing MAO, mao.z.aa@zju.edu.cn
Xia HUANG, https://orcid.org/0000-0003-0907-7488
Guan HUANG, https://orcid.org/0009-0003-4640-959X
Shaojie GU, https://orcid.org/0000-0002-3995-3007
Jun DING, https://orcid.org/0000-0001-7762-889X
Yanhong PENG, https://orcid.org/0000-0002-2162-3798
Zebing MAO, https://orcid.org/0000-0002-2944-7151

Received Jan. 14, 2026; Revision accepted June 3, 2026; Crosschecked July 11, 2026

© Zhejiang University Press 2026

fin coordination jointly limit the performance envelope of fish-like robots.

Fish-inspired robots have received increasing research interest. Marchese et al. (2014) proposed a biomimetic robotic fish actuated by gas-driven soft elastomer actuators, in which BCF propulsion was achieved through fluidic elastomer actuators that generated tail bending and oscillatory motion. Building on this design, Katzschmann et al. (2018) introduced a hydraulically driven system that produced tail oscillation by alternately injecting liquid into chambers on both sides of the tail. The communication modules were also integrated to enable remote control with minimal disturbance to natural organisms. Van den Berg (2019) developed a cable-driven biomimetic robotic fish using BCF propulsion via the caudal fin and pectoral fins for balance, where a single motor-driven gear system actuated cables to produce tail motion. Pfeil et al. (2020) presented a soft biomimetic robotic fish based on dielectric elastomer actuators (DEAs), employing a multilayer stacked configuration to increase maximum tail deflection and improve propulsion efficiency and locomotion agility. Li et al. (2021) developed an untethered soft robotic fish for deep-sea exploration that utilized MPF propulsion and an integrated pressure-adaptive structure by embedding electronic components within a flexible silicone matrix. Despite these advances, most existing studies focus primarily on the mechanical design of flexible bodies or caudal fins, while pectoral fins are often implemented as fixed structures for passive balance. This simplification limits the reproduction of the complex kinematics of real fish pectoral fins and restricts underwater locomotion modes. In contrast, biological fish rely on coordinated fin motions, with pectoral fins contributing to thrust generation, posture regulation, vertical maneuvering, and turning. Therefore, developing a biomimetic robotic fish capable of coordinated control between pectoral fins and the caudal fin would enable more realistic fish-like locomotion and improved biological compatibility.

In this paper, we present a grass-carp-inspired pectoral–caudal-fin (PCF) robot that combines BCF and MPF propulsion through a pectoral-fin shape memory alloy (SMA) large-strain actuator and a caudal-fin SMA spring actuator integrated with a compliant, watertight body. To enhance thermal recovery and fatigue behavior, we implement a sealed-cavity liquid-cooling scheme inside the soft body and further integrate onboard control, wireless operation, and a forward-mounted ultrasonic sensor for autonomous obstacle avoidance. Experiments demonstrate that liquid cooling substantially improves response speed and durability, enabling stable multimodal locomotion with improved single-mode performance and reliable underwater obstacle avoidance.

The contributions of this study are threefold. A biomimetic SMA actuation scheme is proposed for the pectoral and caudal fins to improve response speed and durability. A grass-carp-inspired PCF robotic fish is designed based on coordinated BCF–MPF propulsion to enrich locomotion modes and enhance swimming performance. A novel passive thermal management strategy based on a sealed-cavity vegetable-oil cooling system is further developed to accelerate heat dissipation, improve fatigue resistance, and ensure stable long-term actuation.

2 Bioinspired design

Bionic underwater robots are commonly designed by drawing inspiration from both biological morphology and locomotion mechanisms. Fish morphology is closely coupled with locomotion strategies and has evolved to achieve efficient force generation and maneuverability (Peng et al., 2024). Among aquatic animals, fish with fusiform body shapes, such as grass carp, exhibit highly efficient swimming performance and predominantly employ BCF propulsion. Motivated by these characteristics, this study adopts a hybrid propulsion strategy that combines BCF-based caudal propulsion with MPF-assisted maneuvering (Lin et al., 2023).

2.1 Morphological analysis of fish

The proposed robot integrates caudal fin-dominated propulsion with pectoral fin-assisted control, with particular emphasis on the driving structures of the pectoral fins and the caudal fin. The robot adopts a modular architecture consisting of a head module, a body module, and a tail module (Fig. 1). The head and body modules are fabricated as rigid, watertight shells using polylactic acid (PLA) and material via 3D printing. Their streamlined external geometries follow fish-inspired hydrodynamic profiles, while the elliptical cross-section of the body module reduces hydrodynamic

drag and improves propulsion efficiency. These modules primarily accommodate the control system and provide mounting interfaces for the pectoral fins. The tail module integrates the actuator assembly and the caudal fin, serving as the primary source of propulsive force. A symmetric antagonistic configuration based on SMA actuators is employed to exploit the one-way shape memory effect and enable bidirectional bending through controlled thermal excitation. Heterogeneous elastomeric elements are introduced between adjacent actuator groups to store elastic energy during deformation and assist actuator recovery, thereby improving the dynamic response. Within this configuration, the caudal fin provides the dominant forward thrust, while the pectoral fins generate auxiliary thrust and maneuvering forces.

2.2 Design of the pectoral fin

A typical fish pectoral fin consists of fin rays and an interconnecting fin membrane. Fin rays provide structural support with coupled stiffness and compliance, while the fin membrane ensures coordinated deformation and enhances hydrodynamic interaction with the surrounding fluid. Based on these principles, the biomimetic pectoral fin in this study is constructed using a 0.3 mm thick transparent polymethyl methacrylate (PMMA) plate as the structural substrate. Large-strain SMA actuators are symmetrically arranged on both sides of the substrate to form an antagonistic actuation mechanism. Activation of the SMA actuator on one side induces bending of the substrate and stretching of the opposing actuator, enabling reciprocating flapping motion (Fig. 1b). To improve the force distribution and robustness, each SMA actuator adopts a fin-ray-inspired distributed configuration. A single SMA wire is routed repeatedly between fixed endpoints to form multiple short SMA segments, resulting in more uniform actuation along the fin surface and enhanced fault tolerance. Through this biomimetic design, the pectoral fin effectively reproduces the deformation characteristics of natural fins and provides reliable auxiliary propulsion for the underwater robot. A detailed design is provided in Section S1 of the electronic supplementary materials (ESM).

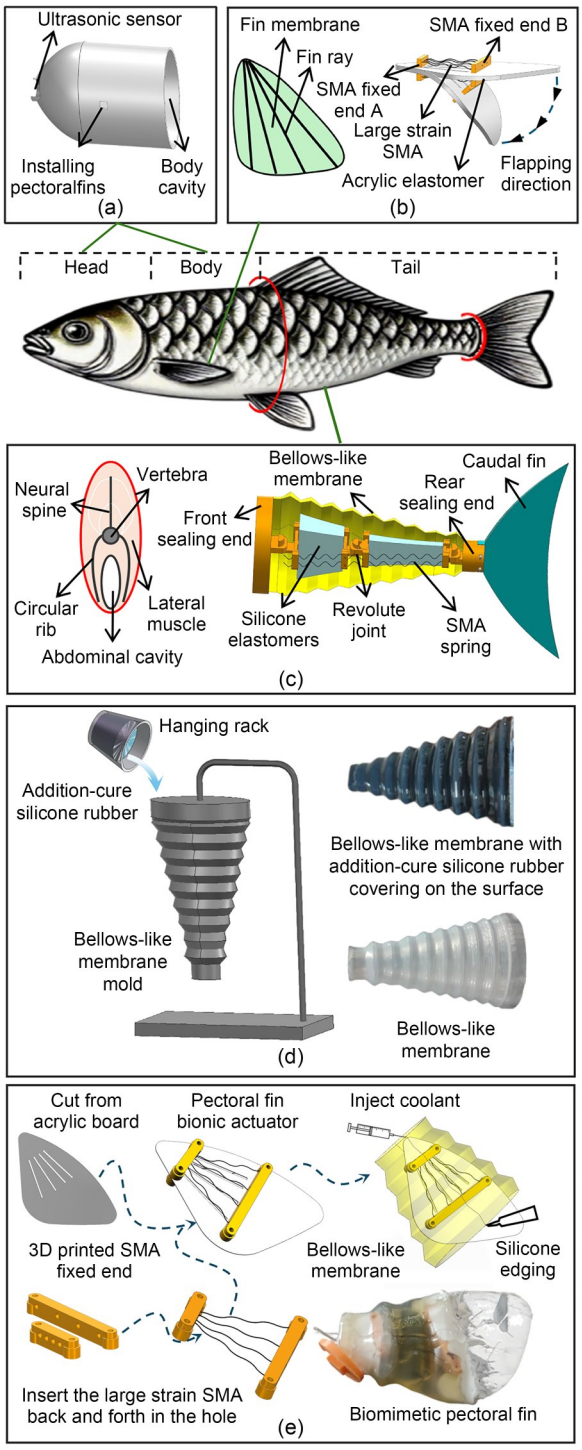


Fig. 1 Bioinspired design: (a) head and body modules; (b) pectoral-fin module; (c) tail module; (d) fabrication process of the bellows-like membrane; (e) fabrication process of the biomimetic pectoral fin

2.3 Design of the caudal fin

Kinematic studies show that grass carp generate propulsive force mainly through periodic lateral oscillations of the posterior one-half to one-third of the body, while the anterior region remains relatively rigid to reduce drag (Cao et al., 2022). The flexible biomimetic

caudal-fin design is shown in Fig. 1c. An AB adhesive sealing plate serves as the structural interface between the elastomeric tail and the internal control module. A bellows-like membrane is bonded to the sealing plate using silicone sealant, forming a sealed cavity. The flexible tail includes a compliant elastomer body and a connector, which provide load-bearing support for SMA spring actuators. The connector uses semicylindrical pins and limit holes, while the elastomer is precision-cast from AB adhesive. After fabrication, SMA springs are prestretched at ambient temperature, routed through the connector, and electrically connected at the proximal end. The bellows-like membrane accommodates large-amplitude bending, maintains sealing under cyclic motion, and provides enclosed space for the cooling medium, ensuring operational reliability in aquatic environments. A detailed design is provided in Section S1 of the ESM.

3 Manufacturing and thermal management strategy

3.1 Bellows-like membrane and waterproof interface

As shown in Fig. 1d, a bellows-like membrane was introduced as the primary deformable waterproof interface of the robot. The membrane was fabricated by a mold-assisted multilayer casting strategy to provide both compliance and sealing reliability under cyclic deformation. Different local thicknesses were adopted in the pectoral-fin and caudal-fin regions according to their distinct deformation demands. In the final system, the membrane not only isolated the internal components from the surrounding water but also formed a sealed cavity for actuator encapsulation and cooling-medium retention. Detailed fabrication conditions and postprocessing procedures are provided in Section S2 of the ESM.

3.2 Actuator materials and structural integration

The pectoral and caudal actuators were designed using different SMA configurations to match their respective functional requirements. As illustrated in Fig. 1e, the pectoral fin employed antagonistically arranged large-strain SMA wires mounted on a 0.3 mm PMMA substrate to achieve lightweight reciprocating flapping. In contrast, the caudal actuator, whose fabrication route is summarized in Figs. 2a and 2b, employed antagonistic SMA springs embedded in a compliant elastomeric tail to generate a larger bending amplitude and higher output force. These material and structural choices were made to balance stiffness, compliance, elastic recovery, structural stability, and underwater durability. Both actuator modules were further packaged as sealed compliant structures so that the passive liquid-cooling medium could be retained within the internal cavity. The structural implementation of the liquid-cooling strategy is therefore embedded directly into the actuator architecture, whereas its thermal effect is experimentally evaluated in Fig. 4. Detailed fabrication, wiring, sealing, and coolant-filling procedures are provided in Section S2 of the ESM.

3.3 Fabrication of rigid components

The rigid head/body shell houses the control electronics, ultrasonic sensor, and fin-mounting interfaces. As shown in Fig. 2c, the body geometry accommodates the pectoral-fin module at the head–body transition

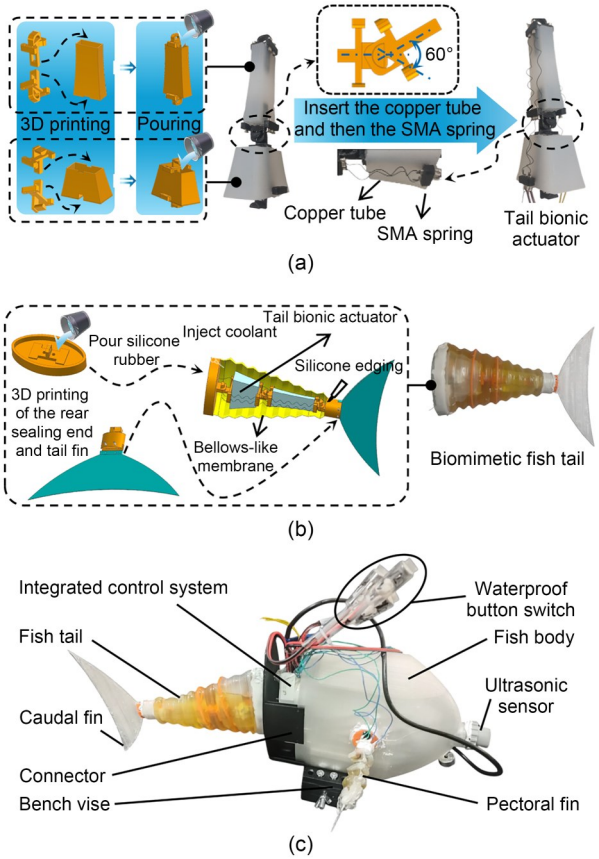


Fig. 2 Fabrication of the robot tail part and assembly: (a) tail soft-body fabrication process; (b) caudal-fin fabrication process; (c) photograph of the assembled robot

while providing a stable mechanical connection to the caudal section. All rigid components were fabricated via 3D modeling followed by monolithic 3D printing, ensuring geometric consistency and facilitating modular integration of the control enclosure. This approach also reduces assembly complexity and improves structural integrity. Additional fabrication details, including material specifications and printing parameters, are provided in Section S2 of the ESM.

3.4 Assembly process of the PCF robot

The structural assembly of the PCF robot follows a modular design philosophy, in which individual functional units are mechanically connected using M2 screws to ensure reliable and repeatable assembly. A photograph of the fully assembled robot is shown in Fig. 2c. From a geometric perspective, the robot has an overall length of (386±0.5) mm, consisting of a 201 mm body module, a 130 mm biomimetic caudal section, and a 55 mm caudal fin. The total width of the robot is (218±0.5) mm, where the main body accounts for 58 mm and each pectoral fin extends to a span of 80 mm on either side. In terms of mass distribution, the total weight of the robot is (721±5) g. The body module, including the integrated control system, weighs 436 g, the combined mass of the bilateral pectoral fins is 74 g, and the biomimetic caudal section accounts for 211 g. A dual-fixation strategy is employed at both the ultrasonic sensor mounting location and the pectoral-fin interfaces. Kafuter K-704N silicone sealant is applied to reinforce mechanical connections while simultaneously providing effective waterproof sealing and enhanced vibration resistance. Detailed assembly workflow, fixation strategy, and sealing implementation are provided in Section S2 of the ESM.

4 Control system

4.1 Hardware architecture of the control system

The control system of the proposed soft robot is composed of several core hardware components, including the power supply units, a central control board, a constant-voltage–constant-current regulation module, a Bluetooth communication module, relays, and an ultrasonic sensor. In terms of power configuration, a dual-voltage supply scheme is adopted to accommodate the heterogeneous electrical requirements of different subsystems. Specifically, the SMA actuators are powered by a 12 V lithium battery to meet their relatively high driving voltage demand, while the control board and auxiliary electronic components are supplied by a separate 5 V lithium battery. A block diagram of the hardware architecture is presented in Fig. 3a.

4.2 Software design of the control system

The software design of the robot control system extends beyond basic swimming commands by integrating ultrasonic sensing to enable autonomous obstacle avoidance in underwater environments (Pan et al., 2025). Compared with 2D LiDAR and depth camera fusion, ultrasonic sensing enables simpler, lower-power, and more robust obstacle avoidance in low-visibility environments (Fan et al., 2024). Switching between different swimming modes is primarily achieved through a Bluetooth connection established between the robot and an upper-level host computer. Once connected, the host computer transmits control commands that are interpreted by the onboard controller. The core control logic is implemented on the Arduino microcontroller, which regulates the on-off states of six relays to control the activation of the SMA actuators, thereby enabling multimodal locomotion of the robot. Specifically, the first and second relays are responsible for controlling the left and right oscillatory motions of the caudal fin, respectively. The third and fifth relays actuate the downward bending and flapping of the left and right pectoral fins, while the fourth and sixth relays control the upward bending motions of the corresponding pectoral fins.

During straight-line cruising, the primary source of propulsion is the oscillatory motion of the biomimetic caudal fin. Consequently, straight swimming can be achieved by alternately activating the first and second relays with equal on-off durations, which generates symmetric left-right tail oscillations and produces forward thrust.

Turning maneuvers are realized using two different motion strategies. In the first strategy, turning is accomplished solely through asymmetric oscillation of the caudal fin, referred to as single-tail-fin turning. For example, during a left turn, the relay controlling the left-side SMA actuator and the relay controlling the right-side SMA actuator are driven with asymmetric heating sequences, as shown in Fig. 3b. A right turn can be achieved by reversing the heating sequence of

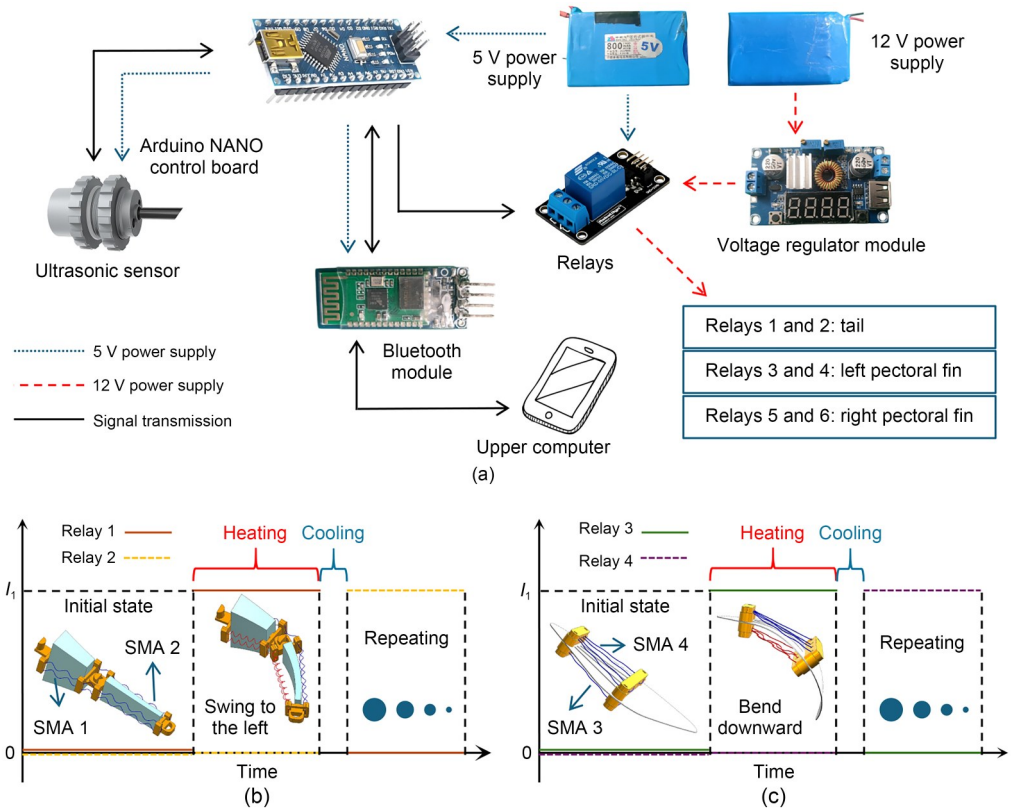


Fig. 3 Control system: (a) system architecture of the liquid-cooled SMA bionic fish. The onboard microcontroller unit receives commands from a Bluetooth module and drives a relay to switch the high-power heating path; (b) single-tail-fin turning via asymmetric caudal-fin oscillation (I_1 is the working current); (c) composite turning via caudal-fin oscillation and pectoral-fin flapping

these two relays. In the second strategy, turning is realized through a composite motion that combines caudal-fin oscillation with coordinated pectoral-fin flapping. During a right turn, for instance, the relays controlling the left pectoral fin are alternately driven at the same frequency to generate asymmetric hydrodynamic forces, as illustrated in Fig. 3c, thereby enhancing turning efficiency and maneuverability.

During autonomous cruising, upon receiving a command from the upper-level host computer via Bluetooth, the control system executes a predefined sequence: all relays switch off, followed by a 0.1 s delay, and then the robot enters autonomous obstacle avoidance mode. In this mode, an ultrasonic sensor continuously monitors forward distance. When the distance exceeds 20 cm, the robot cruises straight; when below 20 cm, it performs a left turn using the caudal fin to avoid the obstacle. The host computer can issue new commands at any time, and the control system prioritizes them by immediately interrupting the current behavior and reconfiguring the relay signals accordingly. This simplified strategy aims to validate the perception–decision–actuation closed loop on an SMA-driven soft robot. Due to size and power constraints, only a single forward-facing sensor is integrated; thus, lateral obstacle distribution cannot be perceived. The left-turn default is chosen based on experimentally validated turning performance, which is approximately symmetric to right turning.

5 Results and discussion

5.1 Thermal management of the actuator

SMA actuator contraction is driven by Joule heating, and ambient temperature directly affects the response rate, making thermal management essential. Cooling strategies fall into two types: passive liquid-assisted and forced cooling. Given the robot's miniaturization and lightweight requirements, passive liquid-assisted cooling was selected to avoid added complexity

and mass. To evaluate different cooling media, heating elements were energized for 0.5 s and then passively cooled. Fluorocarbon compounds resulted in steady-state temperatures above 80 ℃, exceeding the SMA transformation range (Fig. 4a). Deionized water was cooled below 50 ℃, preventing reliable actuation. Vegetable oil offered the best balance: moderate cooling keeps the SMA within its effective range, low dynamic viscosity (0.032 Pa·s) minimally resists motion, and good thermal stability supports long-term operation. MATLAB simulations (Fig. 4b) show that with 1 s heating, the oil temperature rises by about 9 ℃ and reaches thermal equilibrium at 32.7 ℃ within 0.15 s after heating stops. The NiTi SMA wires have an austenite finish temperature of about 32 ℃, enabling effective actuation under this cooling scheme.

To experimentally validate the effectiveness of the selected cooling medium, a fatigue performance test was conducted on the biomimetic fish tail. The experimental platform, illustrated in Fig. 4c, was constructed around an Arduino NANO control board connected to a relay module and an MAX6675 K-type thermocouple module. The controller was programmed with a single-sided heating duration of 0.7 s. The relay output was connected to the power supply and the biomimetic fish tail to form a complete electrical circuit, with the power supply providing an output of 10.4 V and 2.4 A. The thermocouple module was connected to a K-type probe that was positioned at a designated location inside the fish tail during the experiment. Data acquisition was carried out using the built-in serial plotter of the Arduino platform.

Without a cooling medium, the biomimetic fish tail shows good initial performance (Figs. 4d and 4e): the first swing reaches a 23° angle in just 0.3 s. However, the performance rapidly degrades with continued actuation. The reverse swing slows to 0.4 s with a 20° angle. By the third cycle, the swing angle drops to 11° (a 52.2% reduction), and by the fourth cycle, it drops to 8° (65.2% degradation). These results highlight that heat accumulation severely limits fatigue performance and repeatability in the absence of thermal management.

Fig. 4f shows the fatigue performance of the biomimetic fish tail after adding a cooling medium. To assess its effect, the tail was divided axially into three regions: proximal (A), mid (B), and distal (C), with independent temperature monitoring (Fig. 4g). Region C, being spatially constrained, shows the lowest convective heat transfer efficiency and the steepest temperature rise (0.02977 ℃/s). Region B benefits from a sufficient cooling medium and favorable flow, exhibiting a moderate rise rate (0.01276 ℃/s). Region A, with a shorter SMA length and abundant cooling medium, achieves the best thermal management (0.00496 ℃/s).

The relationship between the oscillation amplitude of the fish tail and the time during the first and last 4 s of a 4 min continuous operation is shown in Fig. 4h. The results reveal that within the initial 4 s, the maximum swing angle of the second oscillation cycle increases by 50% compared to the first cycle, which can be attributed to the stabilization of the SMA operating temperature within an effective transformation range during early cycles. More importantly, even after 4 min of continuous operation, the system maintains stable actuation performance, with the maximum swing angle remaining at (6±1)° and the response time stabilized at (0.50±0.02) s. Collectively, these experimental results demonstrate that the cooling medium significantly enhances actuation stability and fatigue resistance during long-term operation.

Fig. 4i presents the time–angle profiles of the pectoral fins under various current excitations. Below 2.4 A, the response is notably sluggish, with a significant increase in the time to reach the maximum deflection angle. Above 2.4 A, no further improvement in actuation performance or maximum angle is observed. Thus, 2.4 A is identified as the optimal excitation current. Although this threshold was determined from tests in air, its validity underwater is supported by the thermal buffering effect of the sealed vegetable-oil cavity and dedicated underwater validation tests (see Section S3 of the ESM for quantitative comparisons).

Fig. 4j illustrates the response characteristics of the biomimetic fish tail in terms of swing angle and angular velocity under different input current conditions. To shorten the cooling interval between tests and improve the experimental efficiency, the tail actuator filled with the cooling medium was tested in an air environment. This test was conducted in air to isolate the intrinsic current–actuation relationship of the SMA actuator while excluding the influence of external hydrodynamic damping. A constant-voltage, variable-current driving strategy was adopted, with the driving voltage fixed at 10.4 V. In each case, the current was maintained until the fish tail reached a steady-state maximum swing amplitude.

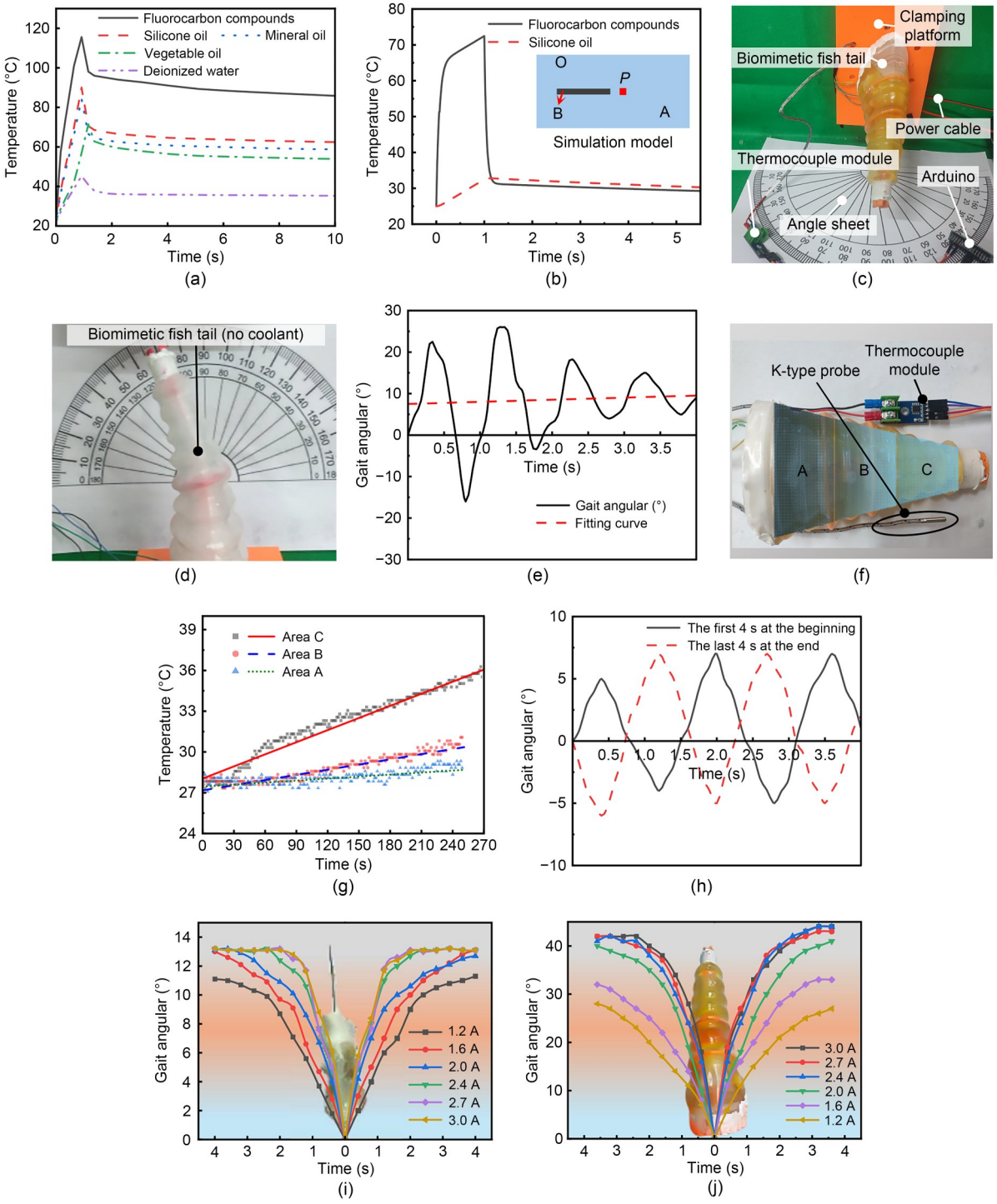


Fig. 4 Thermal management, fatigue performance, and actuation characteristics of the SMA-driven biomimetic robot: (a) temperature decay curve at point *P* under different cooling media; (b) simulated SMA heating and cooling process using different cooling media; (c) experimental setup for SMA fatigue performance testing; (d) fatigue performance of the biomimetic fish tail without cooling medium; (e) temporal evolution of oscillation angle without cooling medium; (f) fatigue performance of the biomimetic fish tail with cooling medium; (g) temperature evolution in different axial regions of the fish tail; (h) comparison of oscillation amplitude at the beginning and end of long-term operation; (i) time–angle response of the pectoral fins under different excitation currents (the positive time axis corresponds to rightward deflection of the pectoral fin, whereas the negative time axis represents leftward deflection); (j) time–angle response of the fish tail under different current inputs

The results clearly indicate that increasing the input current gradually raises the maximum bending angle and angular velocity of the biomimetic fish tail. Below 2.4 A, the response is sluggish, and the tail fails to reach its maximum bending angle quickly. Above 2.4 A, while the swing angle continues to increase, the angular velocity shows little improvement. Thus, an effective current threshold exists at approximately 2.4 A, beyond which the additional current mainly enhances the deformation amplitude rather than the response speed. These component-level results provide qualitative support for the physical plausibility of our simplified models, as the observed trends align with expected analytical descriptions. However, due to the lack of independent parameter identification or quantitative error analysis, these results should not be interpreted as a formal validation of model predictions.

5.2 Basic locomotion modes

Fig. 5a illustrates the indoor underwater experimental platform used to evaluate the robot prototype. The platform consists of an upper-level control terminal, a video recording device, a support frame, the PCF robot, a stainless-steel ruler for scale reference, and a water tank. Both the control terminal and the recording device were implemented using smartphones. The water tank was fabricated from 0.8 cm thick acrylic plates and had overall dimensions of 80 cm in length, 60 cm in width, and 40 cm in height, with a water depth of 25 cm during experiments. In each test, video recording was initiated first, after which motion commands were transmitted to the PCF robot via the control terminal.

Both the pectoral and caudal fins of the biomimetic soft robot serve as actuators during locomotion but exhibit distinct driving characteristics due to different internal SMA configurations. Underwater performance experiments were conducted separately for each actuator type. Based on force-output saturation tests (Section S4 of the ESM), the optimal driving current was determined to be 2.4 A. For straight-line cruising, heating durations between 0.2 and 1.2 s were tested with a fixed cooling time of 0.1 s; a heating duration of 0.4 s achieved a maximum swimming speed of 45.67 mm/s at a stable output frequency of 1 Hz. For turning maneuvers, a heating duration of 0.8 s yielded a minimum turning radius of 19 cm and a maximum angular velocity of 8.86 (°)/s. The 0.1 s cooling time was selected based on thermal and fatigue analyses, which confirmed stable operation for over 200 cycles with an amplitude decay below 10%.

In the present design, straight-line cruising of the PCF robot can be achieved independently by either of the two biomimetic actuators. In Fig. 5b, the tail–straight mode shows the underwater straight-line cruising behavior of the robot driven solely by the caudal fin at a heating frequency of 1 Hz. The results indicate that slight asymmetry in the maximum left and right swing angles of the tail leads to a deviation from an ideal straight trajectory. After 4 s of continuous cruising, the yaw angle reaches approximately 3°, indicating a minor but observable heading deviation. The pectoral–straight mode (Fig. 5b) presents the straight-line cruising process driven by a pair of pectoral fins at the same frequency of 1 Hz. Due to imperfections introduced during the fabrication process, the thrust generated by the two pectoral fins is not perfectly balanced, causing the robot to gradually deviate from the central straight line. After 8 s of continuous motion, the yaw angle increases to approximately 15°, demonstrating a more pronounced deviation than that observed in the caudal-fin-driven case.

Turning is a fundamental locomotion mode for underwater robots, achievable via pectoral fins, the caudal fin, or coordinated control. Observations of fish behavior show that pectoral fins play an auxiliary role, while asymmetric caudal-fin oscillation provides the primary turning torque. In caudal-fin-driven turning, full contraction of one SMA actuator bends the tail into a “C” shape, while partial contraction of the opposite side keeps the tail nearly collinear with the body during recovery (e.g., left turn: left SMA fully contracts and right partially; right turn: opposite). Fig. 5b illustrates this left-turn maneuver. Pectoral-fin turning, in contrast, uses reciprocal flapping of a single fin to generate thrust in the opposite direction, inducing body rotation: a right turn is achieved by actuating the left pectoral fin and vice versa, as shown in Fig. 5b (pectoral–turning mode).

Fig. 5c presents the swimming speed of the robot under different heating sequences. The results reveal a clear trend in which swimming speed increases with increasing heating frequency. When the heating frequency reaches 1 Hz, corresponding to a heating time of 0.4 s, the robot attains its maximum swimming speed. Under these conditions, the pectoral-fin-driven speed reaches 11.25 mm/s, while the caudal-fin-driven

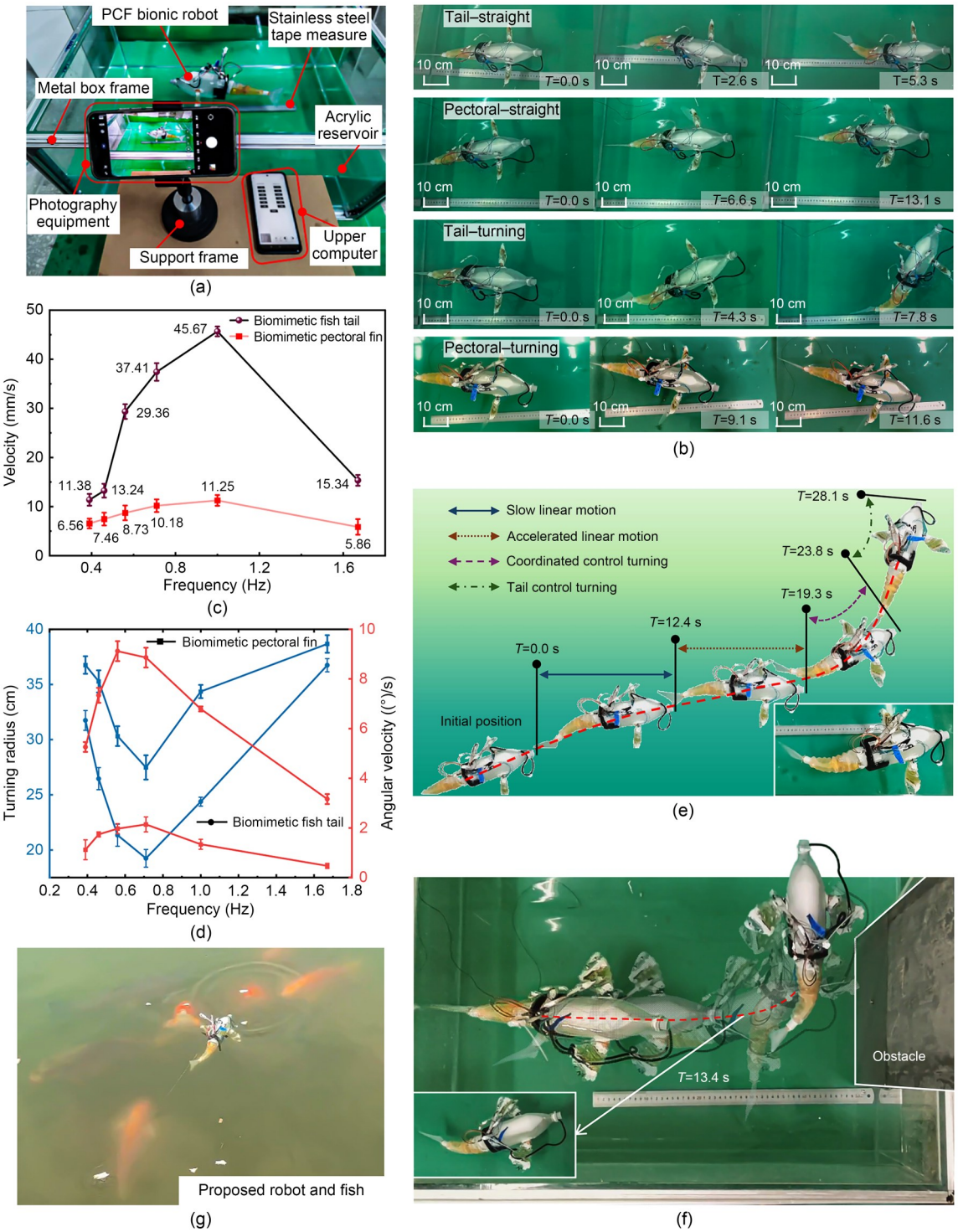


Fig. 5 Basic locomotion modes, multimode motion performance, and environmental interaction experiments of the PCF robot (details are shown in Video S1 of the ESM): (a) indoor underwater experimental platform for locomotion evaluation; (b) basic locomotion modes, including tail-driven straight cruising, pectoral-fin-driven straight cruising, tail-driven turning, and pectoral-fin-driven turning (*T*: time); (c) swimming speed under different heating sequences for pectoral-fin-driven and caudal-fin-driven locomotion (test number *n*=3); (d) turning performance in terms of turning radius and angular velocity under different heating sequences (*n*=3); (e) multimode composite locomotion trajectory achieved through coordinated pectoral- and caudal-fin actuation; (f) autonomous obstacle avoidance trajectory based on ultrasonic sensing; (g) natural environment interaction experiment demonstrating biological compatibility with fish

speed reaches 45.67 mm/s. However, as the heating duration continues to increase and the frequency decreases, the swimming speed exhibits a negative correlation with the heating time. Although longer heating allows the caudal fin to reach its maximum swing angle, the required recovery time also increases, which effectively reduces the oscillation frequency and leads to a lower average swimming speed. Conversely, when the heating time is too short and the frequency is excessively high, the SMA does not complete its phase transformation, resulting in insufficient tail deflection and reduced swimming speed. These observations indicate that the optimal heating time for both the pectoral fins and the caudal fin is 0.4 s, corresponding to a frequency of 1 Hz.

Fig. 5d presents the turning performance under various heating sequences, confirming consistent actuation principles for both pectoral- and caudal-fin driving. The caudal fin, with its large-amplitude oscillation, achieves a smaller turning radius, whereas the pectoral-fin turning resembles rotation about a fixed axis on the non-actuated side but generates lower thrust. For a 90° rotation, pectoral-fin actuation yields a significantly lower angular velocity than caudal-fin actuation. Excessive heating keeps the actuator energized beyond its maximum swing angle, causing the robot to move tangentially along the oscillation arc, which increases the turning radius and reduces the angular velocity. In the current design, the optimal heating time is 0.4 s for straight-line motion (max swimming speed: 45.67 mm/s) and 0.8 s for turning (max angular velocity: 9.12 (°)/s).

Under the optimal straight-line actuation condition (1 Hz, 0.4 s heating), the PCF robot achieves a maximum swimming speed of 45.67 mm/s, corresponding to a normalized speed of 0.118 body lengths per second (BL/s). The Reynolds number is calculated as:

$$Re = \rho LU/\mu = 1.76 \times 10^4,$$

where ρ is the density of water (1000 kg/m^3), L is the characteristic length taken as the overall length of the robot (0.386 m), U is the swimming speed (0.04567 m/s), and μ is the dynamic viscosity of water (1.0×10^{-3} Pa·s). This Reynolds number confirms flow conditions typical of fish swimming and indicates an inertia-dominated flow regime relevant to fish-like cruising. Therefore, the main thrust is primarily generated by momentum transfer associated with caudal-fin oscillation rather than by overcoming viscous shear. The Strouhal number, defined as $St=fA/U$, is found to be 0.31 (with oscillation frequency f=1 Hz, oscillation amplitude A≈0.14 m, and swimming speed U=0.04567 m/s), which falls within the optimal range reported for efficient aquatic locomotion (Triantafyllou et al., 1991). This suggests that the kinematic relationship among oscillation frequency, tail amplitude, and forward speed is hydrodynamically reasonable for efficient thrust production.

From the viewpoint of thrust generation, the caudal fin provides the dominant propulsive force, whereas the pectoral fins contribute auxiliary thrust and stabilizing moments. When the pectoral fins and caudal fin are actuated coordinately, the overall locomotion performance is improved through thrust superposition, wake interaction, and yaw-moment enhancement. This interpretation is consistent with the experimental observation that the multimode mode increased the swimming speed from 45.67 to 51.33 mm/s while also reducing the turning radius from 19 to 15 cm and increasing the angular velocity from 8.86 to 10.20 (°)/s. Moreover, the liquid-cooling strategy indirectly improves locomotion efficiency by maintaining stable oscillation amplitude and thus stable thrust output over long-duration operation. Without cooling, the tail swing angle decayed rapidly from 23° to 8° within four cycles, whereas with vegetable-oil cooling, the robot maintained stable actuation over more than 200 cycles.

5.3 Multimode locomotion

Fig. 5e demonstrates multimode composite motion via coordinated pectoral- and caudal-fin control, achieving a normalized swimming speed of 0.133 BL/s. The motion sequence includes straight-line cruising (1 BL in 10 s), acceleration (second BL in 6 s), a 20° coordinated turn (2 s), and a 40° caudal-fin-only turn (6 s), resulting in smooth and continuous locomotion. As shown in Fig. 5f, an ultrasonic sensor enables autonomous obstacle avoidance with a detection threshold of 20 cm based on the robot's minimum turning radius. When the distance exceeds 20 cm, the robot cruises straight; below 20 cm, it initiates continuous left turns until the path is clear. Experimental results confirm fast avoidance, no collisions, and rapid recovery to straight-line motion after clearing the obstacle.

The complex underwater environment demands high biocompatibility. Equipped with an ultrasonic sensor, the robot achieves autonomous obstacle avoidance, offering a reference for diverse locomotion modes. A

natural interaction experiment in a campus lake, where fish were attracted by bread crumbs, showed that fish continued swimming and feeding near the moving robot without avoidance, demonstrating favorable biocompatibility and potential for harmonious coexistence (Fig. 5g). A transparent fishing line was attached for retrieval. Future research could explore intelligent obstacle avoidance algorithms (Chen et al., 2024; Zeng et al., 2025). Comprehensive comparisons with representative SMA-driven and other smart-material-driven underwater robots are provided in Tables S1–S8 of the ESM. Notably, Table S7 highlights that this work physically validates autonomous obstacle avoidance on an SMA-driven platform while acknowledging the limitations of the current single-sensor, left-turn-priority strategy.

6 Conclusions

We present an SMA-driven underwater biomimetic soft robot with coordinated PCF actuation, addressing key limitations of existing systems in actuation capability, locomotion diversity, and environmental adaptability. First-order physics-based modeling, structural design, thermal management via passive liquid-assisted cooling, control integration, and prototype fabrication were carried out, and the experimental results demonstrated efficient multimode locomotion, enhanced fatigue resistance, and improved maneuverability under optimized driving conditions. The robot achieves robust straight-line cruising, agile turning, coordinated fin-driven motion, and autonomous obstacle avoidance, while natural environment experiments indicate favorable biological compatibility. These results validate the feasibility and effectiveness of SMA-based coordinated actuation for versatile and reliable underwater soft robotic applications.

Acknowledgments

This work is supported by the Chongqing Municipal Human Resources and Social Security Bureau (No. CSTB2025 YCJH-KYXM0046), the Young Project of Science and Technology Research Program of Chongqing Education Commission of China (No. KJQN202501166), the Institute of Light Metals (ILM) Joint Usage/Research Grant, Kumamoto University and University of Toyama (No. 2026-2-K12), the Innovative Research Group of Chongqing Municipal Education Commission (No. CXQT19026), the Cooperative Project between Chinese Academy of Sciences and Universities in Chongqing (No. HZ2021011), the Research Startup Fund of Chongqing University of Technology (No. 0119240197), the Independent Research Project of the State Key Laboratory of Fluid Power and Mechatronic Systems (No. SKLoFP_ZZ_2513), China.

Author contributions

Xia HUANG designed the research. Zhigang DING and Shaojie GU processed the corresponding data. Xia HUANG, Guan HUANG, and Yanhong PENG wrote the first draft of the manuscript. Zebing MAO and Jun DING helped organize the manuscript. Guan HUANG and Yanhong PENG revised and edited the final version of the manuscript. All authors reviewed and approved the final manuscript.

Conflict of interest

Xia HUANG, Guan HUANG, Zhigang DING, Shaojie GU, Jun DING, Yanhong PENG, and Zebing MAO declare that they have no conflict of interest.

Declaration on the use of generative AI tools

ChatGPT was used only for grammar checking during the preparation of this manuscript. No generative AI tools were used to generate scientific content, analyze data, or draw conclusions. The authors reviewed and edited the content as needed and take full responsibility for the content of the publication.

Data availability

The data that support the findings of this study are available from the corresponding author upon reasonable request.

References

Cao YL, Li HQ, Li A, et al., 2022. Structure design and dynamic analysis of a tensegrity-based carangiform robotic fish. *Chinese Science Bulletin*, 67(35):4251-4262. https://doi.org/10.1360/TB-2022-0603

Chen MZ, Liu Y, Zhu DQ, et al., 2024. Parameter identification of an open-frame underwater vehicle based on numerical simulation and quantum particle swarm optimization. *Intelligence & Robotics*, 4(2):216-229. https://doi.org/10.20517/ir.2024.14

Chutia S, Kakoty NM, Deka D, 2017. A review of underwater robotics, navigation, sensing techniques and applications. Proceedings of the 3rd International Conference on Advances in Robotics, article 8. https://doi.org/10.1145/3132446.3134872

Cui Z, Li L, Wang YH, et al., 2023. Review of research and control technology of underwater bionic robots. *Intelligent Marine Technology and Systems*, 1(1):143. https://doi.org/10.1007/s44295-023-00010-3

Ding H, Gao Q, Zhu YW, et al., 2024. Experimental study on navigation performance of bionic underwater vehicle inspired by sea turtle. *Ocean Engineering*, 310:118700. https://doi.org/10.1016/j.oceaneng.2024.118700

Fan BL, Zhao H, Meng LB, 2024. Obstacle detection for intelligent robots based on the fusion of 2D LiDAR and depth

camera. *International Journal of Hydromechatronics*, 7(1): 67-88. https://doi.org/10.1504/ijhm.2024.10060856

Huang X, Xiang HM, Wu C, et al., 2026. CRAB-EDM: a multimodal underwater crab-inspired robot with temporally sequenced electro-discharge modulation. *IEEE Robotics and Automation Letters*, 11(4):3939-3946. https://doi.org/10.1109/LRA.2026.3663817

Katzschmann RK, DelPreto J, MacCurdy R, et al., 2018. Exploration of underwater life with an acoustically controlled soft robotic fish. *Science Robotics*, 3(16):eaar3449. https://doi.org/10.1126/scirobotics.aar3449

Li B, Wang QY, Yu TH, et al., 2026. Quad-wing FWMAV with thrust vector yaw steering. *Biomimetic Intelligence and Robotics*, 6(3):100327. https://doi.org/10.1016/j.birob.2026.100327

Li GR, Chen XP, Zhou FH, et al., 2021. Self-powered soft robot in the Mariana Trench. *Nature*, 591(7848):66-71. https://doi.org/10.1038/s41586-020-03153-z

Li Y, Xu YT, Wu ZG, et al., 2022. A comprehensive review on fish-inspired robots. *International Journal of Advanced Robotic Systems*, 19(3):17298806221103707. https://doi.org/10.1177/17298806221103707

Lin ZL, Zheng W, Zhang JH, et al., 2023. Mudskipper-inspired amphibious robotic fish enhances locomotion performance by pectoral-caudal fins coordination. *Cell Reports Physical Science*, 4(10):101589. https://doi.org/10.1016/j.xcrp.2023.101589

Liu JH, Shen MJ, Ma ZQ, et al., 2024. Research progress on bionic water strider robots. *Journal of Bionic Engineering*, 21(2):635-652. https://doi.org/10.1007/s42235-023-00467-2

Liu RN, Hu XZ, Jiang ZH, et al., 2025. Survey on heterogeneous aquatic robot systems: communication, perception, navigation, control, decision-making and energy management. *Robot Learning*, 2(1):1-61. https://doi.org/10.55092/rl20250003

Liu X, Zhang JH, Li Z, et al., 2025. Design and modelling of multiple-air-chamber pneumatic soft bending actuators. *International Journal of Hydromechatronics*, 8(1):29-50. https://doi.org/10.1504/IJHM.2025.144940

Mao ZB, Suzuki S, Nabae H, et al., 2025. Machine learning-enhanced soft robotic system inspired by rectal functions to investigate fecal incontinence. *Bio-Design and Manufacturing*, 8(3):482-494. https://doi.org/10.1631/bdm.2400152

Marchese AD, Onal CD, Rus D, 2014. Autonomous soft robotic fish capable of escape maneuvers using fluidic elastomer actuators. *Soft Robotics*, 1(1):75-87. https://doi.org/10.1089/soro.2013.0009

Nauert F, Kampmann P, 2023. Inspection and maintenance of industrial infrastructure with autonomous underwater robots. *Frontiers in Robotics and AI*, 10:1240276. https://doi.org/10.3389/frobt.2023.1240276

Pan XW, Xiang S, Niu SL, et al., 2025. Multi-task learning for underwater robot via progressive neural network. *Robot Learning*, 2(2):1-27. https://doi.org/10.55092/rl20250009

Peng YH, Nabae H, Funabora Y, et al., 2024. Controlling a peristaltic robot inspired by inchworms. *Biomimetic Intelligence and Robotics*, 4(1):100146. https://doi.org/10.1016/j.birob.2024.100146

Peng YH, Sakai Y, Funabora Y, et al., 2025. Funabot-Sleeve: a wearable device employing McKibben artificial muscles for haptic sensation in the forearm. *IEEE Robotics and Automation Letters*, 10(2):1944-1951. https://doi.org/10.1109/LRA.2025.3528229

Peng YH, Jiang Y, Zuo ZH, et al., 2026. A rehabilitation design concept based on brain-computer interface and McKibben artificial muscle. *Healthcare and Rehabilitation*, 2(1):100066. https://doi.org/10.1016/j.hcr.2026.100066

Pfeil S, Katzer K, Kanan A, et al., 2020. A biomimetic fish fin-like robot based on textile reinforced silicone. *Micromachines*, 11(3):298. https://doi.org/10.3390/mi11030298

Sahoo SK, Choudhury BB, Dhal PR, 2024. Exploring the role of robotics in maritime technology: innovations, challenges, and future prospects. *Spectrum of Mechanical Engineering and Operational Research*, 1(1):159-176. https://doi.org/10.31181/smeor11202414

Sfakiotakis M, Lane DM, Davies JBC, 1999. Review of fish swimming modes for aquatic locomotion. *IEEE Journal of Oceanic Engineering*, 24(2):237-252. https://doi.org/10.1109/48.757275

Sheng YX, Nie W, Liu Z, et al., 2025. Biomimetic robotics and intelligence: a survey. *SmartBot*, 1(2):e12010. https://doi.org/10.1002/smb2.12010

Triantafyllou MS, Triantafyllou GS, Gopalkrishnan R, 1991. Wake mechanics for thrust generation in oscillating foils. *Physics of Fluids A: Fluid Dynamics*, 3(12):2835-2837. https://doi.org/10.1063/1.858173

van den Berg S, 2019. Design of a High Speed Soft Robotic Fish. Delft University of Technology, Delft, the Netherlands.

Varnousfaderani RH, Estarki M, Zareinejad M, et al., 2025. Lateral undulation and force prediction in soft robotic fish: a systematic approach. *Journal of Bionic Engineering*, 22(6): 2950-2964. https://doi.org/10.1007/s42235-025-00786-6

Wang LS, Shen L, Yi JH, et al., 2026. Prediction model of dynamic fracture toughness of nickel-based alloys: combination of data-driven and multi-scale modelling. *European Journal of Mechanics-A/Solids*, 116:105892. https://doi.org/10.1016/j.euromechsol.2025.105892

Xanthidis M, Joshi B, O'Kane JM, et al., 2022. Multi-robot exploration of underwater structures. *IFAC-PapersOnLine*, 55(31):395-400. https://doi.org/10.1016/j.ifacol.2022.10.460

Zeng TH, Zhu DQ, Gu CH, et al., 2025. An effective fault-tolerant control with slime mold algorithm for unmanned underwater vehicle. *Intelligence & Robotics*, 5(2):276-291. https://doi.org/10.20517/ir.2025.14

Electronic supplementary materials

Sections S1–S4, Tables S1–S8, Video S1